Long Short Term Memory Networks (LSTM)-Monte-Carlo Simulation of Surface Ionization using Radon

Ahmad Muhammed

Firat University

Fatih Külahcı (✉ fatihkulahci@firat.edu.tr)

Firat University   https://orcid.org/0000-0001-6566-4308

Hemn Salh

Firat University; Koya University

Pishtiwan Akram Hama Rashid

Firat University

Research Article

Abstract

Earthquake events are usually associated with the atmospheric processes modification. Some of the important events in seismic periods include the atmospheric electricity/conductivity modification, which is often related to the ion population in the earthquake preparation area vicinity. Radon, together with cosmic radiation is the major ionization sources in the lower troposphere. The ion-pair production rate is estimated as caused by radon in Erzincan, a city along the North Anatolian Fault Zone, Turkey. Long short term memory and Monte Carlo methods are proposed to account for uncertainty in the estimations and also in the radon data to simulate the ion production rate. The advantage of the LSTM model is taken to study radon anomalies during the M=5 Girlevik earthquake, Erzincan. Radon concentration in Erzincan is found to be very high when compared to other regions, and this might relate to the geological settings of the region. Radon concentration is found to increase prior to the 5.0 Girlevik earthquake. According to estimations, $23×10^9$ ion-pairs $m^{-3}s^{-1}$ were generated during the earthquake. The ion production estimation rate due to radon and its progeny in Erzincan is at the order of 10^9 ion-pairs $m^{-3}s^{-1}$. When added to other ionization sources more pronounced conditions could favor ionospheric perturbations. Ionospheric disturbance simulations would be significant in regions with high radon concentration for understanding atmospheric processes.

1.0 Introduction

The lower part of the atmosphere (troposphere), especially near the crustal surface is a key region for the manifestation of lithosphere-atmospheric phenomenon. The term "surface ionization" in this article refers to the production of ions near Earth's crustal surface. One of the inherent events which occur in this region of the atmosphere is the ionization of air molecules, and this comes from various sources. Some of which are radon and its decay products, gamma emission from the ground, and cosmic radiation. In some cases, artificial systems or other external radiation sources contribute to such phenomena (Hirsikko et al., 2011). For example, cosmic radiation contributes to about twenty percent of near Earth's surface ionization (Harrison and Carslaw, 2003), while radioactive decays, in which radon is dominant, contribute to more than 70% of the remaining sources (Warden et al., 2019). The continuous decay and variation of these radioactive elements in atmosphere result in air ionization (especially under favorable conditions), which would populate a given locality with charged aerosols and ions, resulting in the modification of atmospheric electric properties (Anderson and Larson, 1974; Pulinets et al., 2006; Omori et al., 2007; Boldyreff et al., 2013). The parameters involved in modeling electrical processes often depend directly or in directly on ion population for a given region. Without the ion production rate, these models would have to rely on empirical assumptions for most atmospheric electro-dynamic variables, resulting in outcomes, which are not very robust. For example, Denisenko et al. (2008) assumed empirical values while investigating conductivity variations on the penetration of an electrostatic field from the Earth's surface into the ionosphere. Their results would be more realistic with consideration to estimate the values of these electro-dynamic variables using numerical data. Although in most cases it is difficult to get sufficient atmospheric electric data for the simulation, there are other ways (e.g. using radon and cosmic

data), which would enable researchers at least to improve simulation results when incorporated. For instance, the results presented by Xu et al. (2015) turned out to be more plausible for they have incorporated radon exhalation in seismic-ionospheric disturbances modeling.

Radon is a major player in lower surface ionization (Anisimov et al., 2017), and it is constantly exhaled into the atmosphere, especially near fault lines. Its exhalation can vary depending on the geochemistry of a given region (Külahcı and Şen, 2014). Though the mechanism is not fully established, radon concentration can increase (Erees et al., 2007) or decrease (Omori et al., 2007) in relation to seismic activities. In seismic periods, gasses like methane, carbon dioxide, hydrogen, helium and radon are exhaled, and can modify lower atmospheric processes (Pulinets, 2004; Sorokin et al., 2007). As for radon, it ionizes the environment while it decays. This enhances the generation of charged aerosols, ion cluster formation, as well as other nucleation processes. Radon exhalation and atmospheric aerosols dynamics play a great role in understanding atmospheric electrical processes, especially in the study of seismic-ionospheric coupling (Namgaladze et al., 2018; Namgaladze and Karpov, 2015; Pulinets, 2012). Model estimates were presented focusing on the contribution of cosmic radiation to lower tropospheric ionization (Bazilevskaya et al., 2008).

Herein, a simple approach is suggested to study radon contribution in lower atmospheric modification near fault regions. Classical estimations would have inherent uncertainties due to single values, which they produce and therefore, Monte-Carlo simulation method is employed to estimate and quantify ionization caused by radon and its progeny in Erzincan, a city along the North Anatolian Fault zone (NAFZ), Turkey. In Section 2 the procedure is discussed for radon estimation and contribution to surface ionization (ionization near Earth's surface), as well as in the study area and radon data collection methods. Section 3 presents the discussion about the results including the ions produced in radon anomaly periods. Finally, section 4 consists of the findings and their conclusive presentation.

2.0 Radon Ionization

2.1 Study area and Data collection

Turkey is generally considered to be an earthquake-prone area, which is a part of the Tethyan orogenic belt at the junction of three active tectonic plates, which are the Arabian, African and Eurasian plates. Within Turkey there are three main active faults, namely, East Anatolian, North Anatolian, and Bitlis-Zagros suture (Esat et al., 2021). North Anatolian Fault (NAF) begins in the Karlıova region and extends from eastern to western Turkey until the Gulf of Saros along 1,200 km length (Turk et al., 2012). There have been several major earthquakes in these areas close to the NAF over the past hundred years. For example, a magnitude 7.9 earthquake took place at Erzincan (near study region) in 1939, and in 1999 another devastating earthquake occurred at Kocaeli with a magnitude 7.4 (Günay et al., 2018). Radon data used in this study is collected from Erzincan monitoring station. This station is located at (39.7337, 39.61722) latitude-longitude coordinates, Erzincan, Turkey. The soil radon data is given in $kBqm^{-3}$ and recorded in 15-min intervals. AlphaMeter 611 sensors manufactured by AlphaNuclear Co. (Canada) are

used for the continuous monitoring. The AlphaMeter 611sensors were installed at a shallow borehole (1 m) and covered by soil. The daily mean values are used to ease the simulation expenses. The data is collected from (AFAD, Republic of Turkish, Ministry of Interior Disaster and Emergency Management Presidency (https://en.afad.gov.tr/). Earthquake data is from Kandilli Observatory and Earthquake-Tsunami monitoring center, Bogazici University (http://www.koeri.boun.edu.tr/sismo/2/earthquake-catalog/).

2.2 Simulation and anomaly detection

2.2.1 Radon induced Ionization

There are other ionization sources that are significant for consideration in surface ion production rate studies. Since the NAF is seismically active, and radon is one of the prominent tropospheric ionization sources alone the radon contribution to surface ionization combined with cosmic radiation in Erzincan. The choice of ^{222}Rn data has two reasons: First, thoron data is not available for this region. Secondly, radon has a longer half-life compared to thoron then its contribution to air ionization will be prevalent. Radon and cosmic radiation dominate the ion pair production processes in the near ground area of the study region, and the total ion pair production rate (ions-pairs m^{-3}s^{-1}) is given as,

$$q = q_{Rn} + q_{\cos mic} \qquad (1)$$

The contributions from actinon (^{219}Rn) and thoron (^{220}Rn) are excluded in this study, because they are present in trace amounts naturally and have remarkably shorter half-lives (3.96 s for actinon and 55.6 s for thoron) than ^{222}Rn, which hardly permits them enough time to migrate out of the ground, especially in the case of actinon (Chen et al., 2016). Ion production due to cosmic radiation is estimated by the same empirical relation described by various authors (Anisimov et al., 2017; Makino and Ogawa, 1985; Tinsley and Zhou, 2006). The relation yields at sea level as a function of latitude angle (39.7337 for Erzincan). The ion production by radon and its decay products is expressed as the ratio of the total alpha/beta particle energy released by radon (eVm^{-3}s^{-1}) and its progeny and the energy required to produce an ion pair (32-35.6) (Omori et al., 2007; Xu et al., 2015).

$$q_{Rn} = \frac{5.49 \times 10^6 C_{Rn} + 6 \times 10^6 C_{218_{Po}} + 7.69 \times 10^6 C_{214_{Po}}}{35} \qquad (2)$$

where, $C_{Rn}, C_{218_{Po}} \& C_{214_{Po}}$ are respectively the exhaled soil radon, polonium-218, and polonium-214 concentrations.

2.2.2 Data and LSTM simulation

According to radon anomaly criteria, the relationship between earthquake influence radius $R=10^{0.43M}$ (M is earthquake magnitude), and the distance from radon monitoring station to the epicenter should satisfy Eqn. (3) (Dobrovolsky et al., 1979). Both and are in kilometers, is estimated in a similar way as that in Alam et al., (2020).

$$\frac{R}{D_e} \geq 1 \tag{3}$$

The data used for calculations has recorded at 335 observation points from 19th January to December 19th 2009. There are no missing data during the observation periods. In order to simulate the ion production rate, there is a need to establish a convenient model, which would capture and reasonably predict the radon variations (Figure 1).

Radon data is quite irregular with multiple patterns, which would require a robust model, and therefore, the Long Short Term Memory networks (LSTM) is adapted to model the radon time series data. LSTM networks are deep learning models capable of handling data of this nature. They are also capable for retaining the long short-term properties of a sequential data. Predictions made by LSTM is not only dependent on the recent history, every prediction depends on both past as well as present history. Herein the model is designed such that it does not t over fit the data. The process involves adding/reducing dense-layers, dropouts, prediction parameters, neurons, etc. The model structure is modified continuously until the best outcome is attained. More detailed information can be found on LSTMs in (Nazaroff, 1992; Singh, 2017; Xiao, 2020; Chen et al., 2021).

For the implementation of LSTM on radon time series, Keras (https://keras.io/) is employed with Tensorflow backend (https://www.tensorflow.org). Keras is a user-friendly API (Application Programming Interface) designed for implementation of machine learning models. The LSTM architecture used to model radon time series consists of an LSTM input layer, a dropout layer and an output dense layer. The LSTM input layer usually expects a 3D input samples, window slide and features. The window slide is the length of each slice in the sample sequence, which is chosen as 4. The final dimension is the feature, and is set to 1 since there is no other data (e.g. temperature) besides radon. By default, the LSTM input layer assumes the existence of one or more sample data sets. Hence, only the window and feature inputs are necessary with assignment of 99 neurons to the input layer, which means 99 outputs. "*relu*" activation function is used to activate the LSTM layer in each EPOCH. The second is the dropout layer, which randomly drops some neurons during the LSTM training period. It helps to prevent over fitting and enables the network to better generalize the data. The dropout rate is set to 28%, and its output is finally fed into the output dense layer, which then gives the final radon prediction. The supervised learning tradition requires the radon data in the form of input and target arrays. Herein, 70% of the data is used for training (19th March 2007 to 11th February 2008), and 30% for testing (3rd March 2008 to 15th August 2008). The model is trained for 99 EPOCHS, and "*adam*" optimizer is used to optimize the model during

the training. Finally, the mean square error is chosen as the loss function, and 25% of the training data is used for validation during the training period.

2.2.3 Radon anomaly detection

LSTMs also plays a role in anomaly detection, especially for time series data (Bontemps et al., 2017; Malhotra et al., 2016; Siingh et al., 2007). The scaled residual is expressed as,

$$\left(SR = \frac{LSTM - Radon}{Radon} \right) \tag{4}$$

The purpose of scaled residual is to detect radon anomalies for the training fit and forecast regions. The anomaly condition is set such that radon observation would be considered as an anomaly if its corresponding falls beyond *Residual Mean*$\pm 1.96\sigma_{SR}$, where σ is the standard deviation of the scaled residual. This method requires that, the LSTM model fits the data quite well such that the fit error is normally distributed with good covariance. Since radon anomaly is often associated with seismicity, and the study region is seismically active, the possibly detected anomalies is analyzed in relation to the earthquake, which occurred in Girlevik, a district around Erzincan. Girlevik is only 14 km from radon monitoring station. The earthquake is very shallow (3 km depth), it has a magnitude , and with a 141 km preparation radius. Its epicentral coordinates are (39.60, 39.75). The earthquake occurred on 30th July 2009, 7:37 a.m. universal time, and it satisfies Eqn. (3) (Alam et al., 2020).

2.2.4 Monte-Carlo Simulation

radon simulation is the main purpose to know the contribution to surface ionization, and therefore, the use of radon average value, means a lot of information has been truncated. For better simulation there is the need to compensate the lost information. Monte-Carlo method is a significant tool when dealing with uncertainty in predictions, and would be a best candidate approach for this task (Şen, 2019). The Monte-Carlo simulation is implemented for the LSTM fit on radon time series to simulate surface ionization rate. Radon data is simulated within of the LSTM prediction curve, the simulation is for 99 paths, Eqn. (2) is then estimated for each path. The Monte-Carlo simulation approach is adopted from Muhammad et al. (2020) with a. difference that instead of generating the paths directly, the rolling mean of the paths is computed for all 99 simulations. The purpose is to have most of the simulations centralized not far from the prediction curve. Monte-Carlo mean simulation is tracked for performance at each training EPOCH, which is done by computing the root mean square error (RMSE), the coefficient of variation (R^2), and its Pearson correlation coefficient with the real radon data.

3.0 Results
3.1 Radon and LSTM model

The fit results for the training region (Figure 2, A-panel) indicate a linear relationship between radon and the LSTM model, because the data is concentrated near the regression line. In addition, the Pearson's correlation (R^2) value of about 93% suggests good training fit by the LSTM, which means the dropout layer was successful in deterring model over-fitting. On the right panel (Figure 2, B-panel), the training residuals are available, which nearly fit a theoretical normal distribution with slight deviations on the tail. The overall training RMSE is about 4.8 kBqm^{-3}, and the R^2 value is shown in Figure 2, where C-panel suggests that the model would account for 84% of radon variation, and this implies a decent forecast. The linearity relationship is visually clear from the scatter plot in Figure 2, C-panel. The data is centered on the regression curve, but a little sparse when compared to the training. The Q-Q plot in D-panel gives the impression that the forecast residuals fit a theoretical normal distribution, inferring reasonable forecast and the forecast RMSE value is 5.3 kBqm^{-3}, that the radon data is close to the LSTM predictions. However, the outliers in Figure 2, A&C could possibly be the result of an external factor influencing radon variation, which could be meteorological or geological (seismic). The outliers show that the model does not over fit the data despite its good performance. This was another uncertainty in estimation, and therefore, Monte Carlo method is employed accounting.

3.2 Radon and Ion production rate

Table 1 gives the statistical properties of radon (row 1), ion production due to radon alone (row 2), and ion production due to radon and cosmic radiation (last row). It is good to bear in mind that those units of the ion production rates are also of the order of 10^3 "k" since they would automatically be affected by radon units. Radon concentration has a mean of 29 kBqm^{-3}, which is the maximum value (74 kBqm^{-3}) during summer/early autumn, and obviously a minimum (5 kBqm^{-3}) during the winter, mid-spring or late Autumn seasons. Similar variations have been reported in literature (Kikaj et al., 2016; Muhammad et al., 2020). These radon values are rarely reported in places without seismic activity. For example, Fijałkowska-Lichwa and Przylibski, (2016) reported that radon values remain between 0.8 to 1.2 kBqm^{-3} in an underground geodynamic laboratory in Poland. Richon et al., (2007) reported soil radon variations ranging from 4 to 24 kBqm^{-3} in a long term soil radon monitoring along the rift of Corinth in Greece. They recorded abrupt anomalies, which they believed could be seismically induced. On the other hand, Font et al., (2008) reported radon values as high as 140 kBqm^{-3} in a study along the Amer Fault, Barcelona. More can be found in Baskaran (2016). These examples are only given to support the argument that radon concentrations are higher near the faults than in aseismic regions. However, some regions are aseismic, but exceptionally rich in radon concentration (e.g. Mentes and Eper-Pápai, 2015).

The ion production was first estimated using raw radon daily mean, and then it is simulated using the LSTM model for 99 different paths. The estimations of raw radon are given in the second row of Table 1 and ion production ranges between 0.3 to 2.8×10^{10} ion-pairs m^{-3}s^{-1} respectively. This suggests high radon induced ionization levels in the region. However, this is no surprise since even the soil radon concentration levels are high with the mean ion production due to radon is about 11×10^9 ion-pairs m^{-3}s^{-1}

which is almost similar, but 10^3 higher in magnitude compared to the estimations by Xu et al., (2015). A Similar 10^3 order difference is obtained from the comparison of the estimated ionization caused by our 10 kBqm^{-3} to the estimations made Omori et al (2007). The reason for this difference is that, both cited authors have their radon concentrations in Bqm^{-3} while it is kBqm^{-3} in this study.

Further comparison of the estimations from Eqn. (2) and the experimentally measured ionization caused by the anomalous Mexico 300-400 Bqm^{-3} radon as mentioned by Pulinets et al. (2006). It is shown in this study that the ion-pair production estimation rates could probably be exaggerated. However, uncertainties are addressed using Monte-Carlo (see Figure 3). With the aid of Monte-Carlo, 99 simulation paths are generated for each estimated ion-pair production. It would be worthy to note that Monte Carlo method is applied only to account for uncertainty in estimations. The aim is to simulate all possible radon values, which would yield different outcomes for the ion production rate. The mechanism is simple, sampling randomly from the training residual, and adding to the LSTM prediction/forecast path. Hence, a distinct outcome is generated for each simulation. The Monte Carlo paths generations are rejected whenever they cross the prediction bounds.

These simulation paths are believed to have accounted for a range of prediction uncertainties. For example, at least one simulation path each would have covered the values for both Eqn. (1) and Eqn. (2). This is seen when one compares the simulation curves in Figure 3 to that in Figure 5. A-panel no matter the case, the ion pair production rate in this region is high due to high radon concentration. The consequence of this has to do with the geo-chemistry and geological settings of the study area dealing with an active fault zone. These ionization rates occur for each unit meter cube of the study region. With this high ionization rates, the locality of radon monitoring region would be densely populated with ions (ion-pairs cm^{-3}s^{-1}). If meteorological processes are less dominant, a quasi-static electric field would be generated due to the continuous ionization of air molecules by radon and its progeny in the localized region. The process is quasi-static, since there are no convective drives from external sources dominating the movement of generated ions and ion-ion recombination would be the major sink due to less collision with aerosol particles. In this case, any convective/seismic driven flow of ions in vertical direction would result in the generation of extraneous current (Sorokin et al., 2007; Namgaladze et al., 2018). This current generations add to the global electric circuit current, and under enhanced conditions could result in ionospheric perturbations (Sorokin et al., 2020). If the calculations in Xu et al., (2015) were repeated in the Erzincan NAF region with radon data from this study, the estimations for surface ion pair production rate would be 10^3 higher, which means the resulting electric field into the ionosphere due to radon would improve. In this case, the ion production sources are significant in understanding atmospheric electrical properties of a given region. Hence, results from generalized seismic-ionospheric models (global models) would yield more decent and realistic outcomes if localized.

3.3 Ion production in seismic periods

The geological/seismic influences on radon exhalation is more interesting to achieve, because there is the need to filter out meteorological influences. The relationship between radon and soil temperature at 50 cm depth for the study period is significantly positive, with a Pearson's correlation of about 0.76. The same significant positive relationship is obtained with atmospheric temperature (R=0.6). The relationship with atmospheric pressure is weak and negative, the Person's correlation gives a value of about (R= -0.3). These results suggest that any recorded radon anomaly could be attributed to meteorological influences, and therefore, in order to relate radon anomalies with external factors, there is the need for these anomalies to exist where temperature and pressure influences are absent. Figure 4 presents the variation of soil temperature at 50 cm depth (blue solid curve), atmospheric temperature (solid green curve), and atmospheric pressure (solid brown curve) throughout the study period. The dotted lines in each panel indicate a 7-day rolling standard deviation for each parameter.

Meteorological anomalies are classified such that for each set of the computed rolling standard deviation due to outliers by setting a threshold. Any data point very far from the 4th quartile of the data would be considered an outlier. The corresponding position, where it exists is labeled as an anomaly (see dark colored circles in Figure 4). For atmospheric pressure (Figure 4, upper panel), anomalies exist on 9th, 10th, and 11th February 2009, as well as on the 14th of March 2009 (Figure 4, middle panel). The soil temperature anomalies exist on the 4th, 5th and 6th of November 2009 (Figure 4, lower panel). Finally, the atmospheric temperature anomalies occurred on the 8th and 9th of March 2009, and hence, external influences can be regarded when radon anomalies are registered outside these periods.

In search for the geological influence, only one earthquake is considered in this study. The earthquake (Girlevik earthquake, M=5) occurred on 30th July 2009, 7:37 a.m. universal time. Radon and ion pair production variations in these periods are presented in Figure 5 in C-panel, there are three anomaly regions. Two abrupt anomalies are observed on 28th & 30th July and the third one from 5th to 29th August. As mentioned in Section **2.1.2,** the Girlevik earthquake is shallow and satisfies Eqn. (1), and the dates which radon anomalies show do not coincide with dates having meteorological influences. This suggests that the observed radon anomalies can possibly be attributed to factors which are not meteorological.

The labeled pink circles (a, b, & c) in Figure 5(A) mark the variations in ion pair production due to radon (black solid curve), and its combination with cosmic radiation (black dashed curve). In B-panel of Figure 5 radon concentration increased slowly from winter through spring, and then fluctuations begin in July. An abrupt decrease is observed two days away from the main shock (28th July). It is then followed by a sharp increase, reaching at 60.3 kBqm^{-3}. The ion production rate due to radon at this time was about 2.3×10^{10} ion-pairs m^{-3}s^{-1}, this sharp increase in radon concentration is immediately followed by the Girlevik earthquake (30th July 2009, M=5). The observed anomaly on the 28th and prior could be a consequence of crustal adjustments/collisions during preparation leading to instabilities in radon exhalation. While the increase moments and during the shock could be a consequence of crustal pressure driven radon exhalation. The aftershock was followed by a drastic decrease and increase in radon

concentration, which are presented in Table 2. The observed pre seismic radon decrease could possibly relate to the trapping of radon within crustal stress regions, while the post seismic increase could result from pressurized release during crustal stress recovery.

4.0 Conclusion

The ion-pair production rates are estimated caused by radon in Erzincan, a city along the North Anatolian Fault. To account for uncertainty in the estimations, LSTM and Monte Carlo methods are applied on radon data to simulate the ion production rate. The LSTM model is employed to study radon anomalies during the M=5 Girlevik earthquake, Erzincan, where the radon concentration is found to increase prior to the 5.0 Girlevik earthquakes. According to estimations, 23×10^9 ion-pairs $m^{-3}s^{-1}$ were generated during the Earthquake. The estimated ion production rate due to radon and its progeny is of the order of 10^9 ion-pairs $m^{-3}s^{-1}$. Its addition to other ionization sources and in more pronounced conditions could favor ionospheric perturbations. Hence, considering ion production sources in lower atmosphere (especially in regions with high radon concentration) would be significant to understand atmospheric processes like that of seismic-ionospheric coupling.

Declarations

Declaration of competing interest

The authors declare that they have no known competing financial interests or personal relationships that could have appeared to influence the work reported in this paper.

Acknowledgments

References

Alam, A., Wang, N., Zhao, G., Barkat, A., 2020. Implication of Radon Monitoring for Earthquake Surveillance Using Statistical Techniques: A Case Study of Wenchuan Earthquake. Geofluids 2020, 1–14. https://doi.org/10.1155/2020/2429165

Anderson, R. V, Larson, R.E., 1974. Atmospheric electric and radon profiles over a closed basin and the open ocean. J. Geophys. Res. 79, 3432–3435. https://doi.org/10.1029/jc079i024p03432

Anisimov, S. V, Galichenko, S. V, Mareev, E.A., 2017. Electrodynamic properties and height of atmospheric convective boundary layer. Atmos. Res. 194, 119–129. https://doi.org/10.1016/j.atmosres.2017.04.012

Baskaran, M., 2016. Radon: A Tracer for Geological, Geophysical and Geochemical Studies, Radon: A Tracer for Geological, Geophysical and Geochemical Studies. Springer International Publishing. https://doi.org/10.1007/978-3-319-21329-3

Bazilevskaya, G.A., Usoskin, I.G., Flückiger, E.O., Harrison, R.G., Desorgher, L., Bütikofer, R., Krainev, M.B., Makhmutov, V.S., Stozhkov, Y.I., Svirzhevskaya, A.K., Svirzhevsky, N.S., Kovaltsov, G.A., 2008. Cosmic ray induced ion production in the atmosphere. Space Sci. Rev. 137, 149–173. https://doi.org/10.1007/s11214-008-9339-y

Boldyreff, A., Kupovykh, G., Redin, A., 2013. Modeling of ionization-recombination processes in the atmospheric surface layer. J. Electrostat. 71, 305–311. https://doi.org/10.1016/j.elstat.2013.01.004

Bontemps, L., Cao, V.L., McDermott, J., Le-Khac, N.-A., 2017. Collective Anomaly Detection based on Long Short Term Memory Recurrent Neural Network. Lect. Notes Comput. Sci. (including Subser. Lect. Notes Artif. Intell. Lect. Notes Bioinformatics) 10018 LNCS, 141–152.

Chen, W., Xu, H., Jia, L., Gao, Y., 2021. Machine learning model for Bitcoin exchange rate prediction using economic and technology determinants. Int. J. Forecast. 37, 28–43. https://doi.org/10.1016/j.ijforecast.2020.02.008

Chen, X., Kerminen, V.-M., Paatero, J., Paasonen, P., Manninen, H.E., Nieminen, T., Petäjä, T., Kulmala, M., 2016. How do air ions reflect variations in ionising radiation in the lower atmosphere in a boreal forest? Atmos. Chem. Phys. 16, 14297–14315. https://doi.org/10.5194/acp-16-14297-2016

Denisenko, V. V, Boudjada, M.Y., Horn, M., Pomozov, E. V, Biernat, H.K., Schwingenschuh, K., Lammer, H., Prattes, G., Cristea, E., 2008. Ionospheric conductivity effects on electrostatic field penetration into the ionosphere. Nat. Hazards Earth Syst. Sci. 8, 1009–1017. https://doi.org/10.5194/nhess-8-1009-2008

Dobrovolsky, I.P., Zubkov, S.I., Miachkin, V.I., 1979. Estimation of the size of earthquake preparation zones. Pure Appl. Geophys. PAGEOPH 117, 1025–1044. https://doi.org/10.1007/BF00876083

Erees, F.S., Aytas, S., Sac, M.M., Yener, G., Salk, M., 2007. Radon concentrations in thermal waters related to seismic events along faults in the Denizli Basin, Western Turkey. Radiat. Meas. 42, 80–86. https://doi.org/10.1016/j.radmeas.2006.06.003

Esat, K., Seyitoğlu, G., Aktuğ, B., Kaypak, B., Ecevitoğlu, B., 2021. The Northwest Central Anatolian Contractional Area: A neotectonic deformation zone bounded by major strike-slip fault zones in the Anatolian Plate. Tectonophysics 805, 228776. https://doi.org/10.1016/j.tecto.2021.228776

Fijałkowska-Lichwa, L., Przylibski, T.A., 2016. First radon measurements and occupational exposure assessments in underground geodynamic laboratory the Polish Academy of Sciences Space Research Centre in Książ Castle (SW Poland). J. Environ. Radioact. 165, 253–269. https://doi.org/10.1016/j.jenvrad.2016.10.010

Font, L., Baixeras, C., Moreno, V., Bach, J., 2008. Soil radon levels across the Amer fault. Radiat. Meas. 43, S319–S323. https://doi.org/10.1016/j.radmeas.2008.04.072

Günay, O., Saç, M.M., İçhedef, M., Taşköprü, C., 2018. Soil gas radon concentrations along the Ganos Fault (GF). Arab. J. Geosci. 11, 1–5. https://doi.org/10.1007/s12517-018-3542-2

Harrison, R.G., Carslaw, K.S., 2003. Ion-aerosol-cloud processes in the lower atmosphere. Rev. Geophys. 41. https://doi.org/10.1029/2002RG000114

Hirsikko, A., Nieminen, T., Gagné, S., Lehtipalo, K., Manninen, H.E., Ehn, M., Hõrrak, U., Kerminen, V.M., Laakso, L., McMurry, P.H., Mirme, A., Mirme, S., Petäjä, T., Tammet, H., Vakkari, V., Vana, M., Kulmala, M., 2011. Atmospheric ions and nucleation: A review of observations. Atmos. Chem. Phys. 11, 767–798. https://doi.org/10.5194/acp-11-767-2011

Kikaj, D., Jeran, Z., Bahtijari, M., Stegnar, P., 2016. Radon in soil gas in Kosovo. J. Environ. Radioact. 164, 245–252. https://doi.org/10.1016/j.jenvrad.2016.07.037

Külahcı, F., Şen, Z., 2014. On the Correction of Spatial and Statistical Uncertainties in Systematic Measurements of ^{222}Rn for Earthquake Prediction. Surv. Geophys. 35, 449–478. https://doi.org/10.1007/s10712-013-9273-8

Makino, M., Ogawa, T., 1985. Quantitative estimation of global circuit. J. Geophys. Res. 90, 5961. https://doi.org/10.1029/JD090iD04p05961

Malhotra, P., Ramakrishnan, A., Anand, G., Vig, L., Agarwal, P., Shroff, G., 2016. LSTM-based Encoder-Decoder for Multi-sensor Anomaly Detection.

Mentes, G., Eper-Pápai, I., 2015. Investigation of temperature and barometric pressure variation effects on radon concentration in the Sopronbánfalva Geodynamic Observatory, Hungary. J. Environ. Radioact. 149, 64–72. https://doi.org/10.1016/j.jenvrad.2015.07.015

Muhammad, A., Külahcı, F., Akram, P., 2020. Modeling radon time series on the North Anatolian Fault Zone, Turkiye: Fourier transforms and Monte Carlo simulations. Nat. Hazards 104, 979–996. https://doi.org/10.1007/s11069-020-04200-8

Namgaladze, A., Karpov, M., Knyazeva, M., 2018. Aerosols and seismo-ionosphere coupling: A review. J. Atmos. Solar-Terrestrial Phys. 171, 83–93. https://doi.org/10.1016/j.jastp.2018.01.014

Namgaladze, A.A., Karpov, M.I., 2015. Conduction current and extraneous electric current in the global electric circuit. Russ. J. Phys. Chem. B 9, 754–757. https://doi.org/10.1134/S1990793115050231

Nazaroff, W.W., 1992. Radon transport from soil to air. Rev. Geophys. 30, 137–160. https://doi.org/10.1029/92RG00055

Omori, Y., Yasuoka, Y., Nagahama, H., Kawada, Y., Ishikawa, T., Tokonami, S., Shinogi, M., 2007. Anomalous radon emanation linked to preseismic electromagnetic phenomena. Nat. Hazards Earth Syst. Sci. 7, 629–635. https://doi.org/10.5194/nhess-7-629-2007

Pulinets, S., 2012. Low-latitude atmosphere-ionosphere effects initiated by strong earthquakes preparation process. Int. J. Geophys. 2012. https://doi.org/10.1155/2012/131842

Pulinets, S., 2004. Ionospheric precursors of earthquakes: Recent advances in theory and practical applications. Terr. Atmos. Ocean. Sci. 15, 413–435. https://doi.org/10.3319/TAO.2004.15.3.413(EP)

Pulinets, S. A., Ouzounov, D., Ciraolo, L., Singh, R., Cervone, G., Leyva, A., Dunajecka, M., Karelin, A. V., Boyarchuk, K.A., Kotsarenko, A., 2006. Thermal, atmospheric and ionospheric anomalies around the time of the Colima M7.8 earthquake of 21 January 2003. Ann. Geophys. 24, 835–849. https://doi.org/10.5194/angeo-24-835-2006

Pulinets, S A, Ouzounov, D., Karelin, A. V, Boyarchuk, K.A., Pokhmelnykh, L.A., 2006. The physical nature of thermal anomalies observed before strong earthquakes. Phys. Chem. Earth 31, 143–153. https://doi.org/10.1016/j.pce.2006.02.042

Richon, P., Bernard, P., Labed, V., Sabroux, J.C., Beneïto, A., Lucius, D., Abbad, S., Robe, M.C., 2007. Results of monitoring 222Rn in soil gas of the Gulf of Corinth region, Greece. Radiat. Meas. 42, 87–93. https://doi.org/10.1016/j.radmeas.2006.06.013

Şen, Z., 2019. Earth Systems Data Processing and Visualization Using MATLAB. Springer. https://doi.org/10.1007/978-3-030-01542-8

Siingh, D., Gopalakrishnan, V., Singh, R.P., Kamra, A.K., Singh, S., Pant, V., Singh, R., Singh, A.K., 2007. The atmospheric global electric circuit: An overview. Atmos. Res. 84, 91–110. https://doi.org/10.1016/j.atmosres.2006.05.005

Singh, A., 2017. Anomaly Detection for Temporal Data using Long Short-Term Memory (LSTM). Stockholm, Sweden.

Sorokin, V.M., Chmyrev, V.M., Hayakawa, M., 2020. A Review on Electrodynamic Influence of Atmospheric Processes to the Ionosphere. Open J. Earthq. Res. 09, 113–141. https://doi.org/10.4236/ojer.2020.92008

Sorokin, V.M., Yashchenko, A.K., Hayakawa, M., 2007. Electric field perturbation caused by an increase in conductivity related to seismicity-induced atmospheric radioactivity growth. Russ. J. Phys. Chem. B 1, 644–648. https://doi.org/10.1134/s1990793107060206

Tinsley, B.A., Zhou, L., 2006. Initial results of a global circuit model with variable stratospheric and tropospheric aerosols. J. Geophys. Res. Atmos. 111, 1–23. https://doi.org/10.1029/2005JD006988

Turk, T., Gümüşay, U., Tatar, O., 2012. Creating infrastructure for seismic microzonation by Geographical Information Systems (GIS): A case study in the North Anatolian Fault Zone (NAFZ). Comput. Geosci. 43, 167–176. https://doi.org/10.1016/j.cageo.2011.10.006

Warden, S., Bleier, T., Kappler, K., 2019. Long term air ion monitoring in search of pre-earthquake signals. J. Atmos. Solar-Terrestrial Phys. 186, 47–60. https://doi.org/10.1016/j.jastp.2019.01.009

Xiao, F., 2020. Time Series Forecasting with Stacked Long Short-Term Memory Networks.

Xu, T., Zhang, H., Hu, Y., Wu, J., 2015. Electric field penetration into the ionosphere in the presence of anomalous radon emanation. Adv. Sp. Res. 55, 2883–2888. https://doi.org/10.1016/j.asr.2015.03.015

Tables

Table 1

Radon, ion production rate due to Rn, and ion production rate due to Rn and cosmic radiation.

	Count	Mean	Std Dev	Min	25%	50%	75%	Max
Radon (Bqm^{-3})	335	29.0×10^3	18.0×10^3	5.8×10^3	12.3×10^3	24.4×10^3	43.2×10^3	74.1×10^3
(units $\times 10^3$)	335	1.1×10^7	0.6×10^7	0.3×10^7	0.4×10^7	0.9×10^7	1.6×10^7	2.8×10^7
(units $\times 10^3$)	335	1.2×10^7	0.7×10^7	0.4×10^7	0.6×10^7	1.0×10^7	1.8×10^7	3.0×10^7

Table 2 Radon anomalies and corresponding ion production rates

| Date	Positive Anomalies				Negative Anomalies			
	Rn (Bqm^{-3})	(units $\times 10^3$)	Q_{rad_sun}	Relative increase	Rn (Bqm^{-3})	(units $\times 10^3$)	Q_{rad_sun}	Relative decrease
2009-07-28					59.2×10^3	2.3×10^7	2.4×10^7	29%
2009-07-30	60.3×10^3	2.3×10^7	2.5×10^7	19%				
2009-08-05					61.4×10^3	2.4×10^7	2.5×10^7	48%
2009-08-07	63.1×10^3	2.4×10^7	2.6×10^7	25%				
2009-08-12	65.1×10^3	2.5×10^7	2.6×10^7	33%				
2009-08-20	72.3×10^3	2.7×10^7	2.9×10^7	39%				
2009-08-29	67.5×10^3	2.6×10^7	2.8×10^7	23%				

Figures
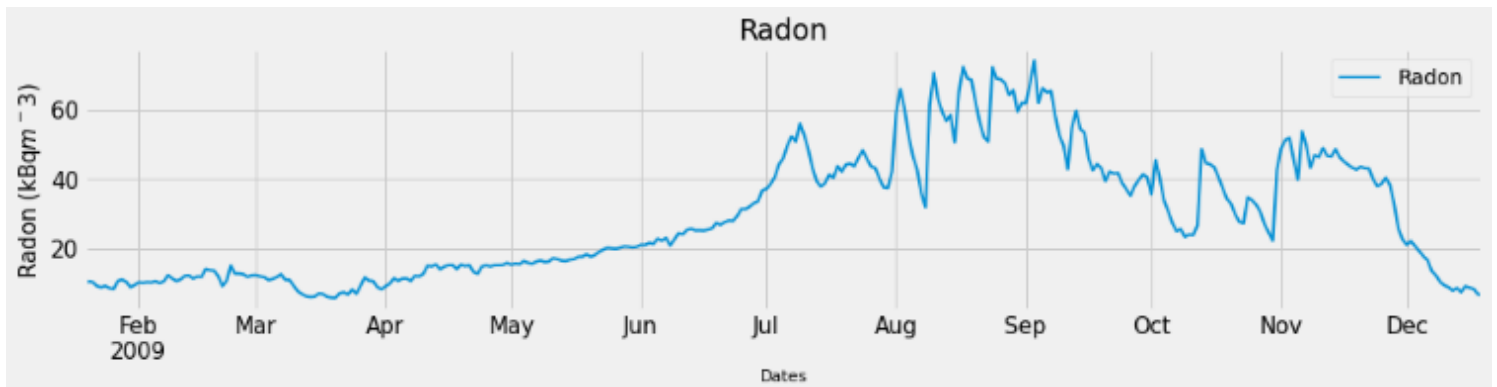
Figure 1

Radon variation during the study period,
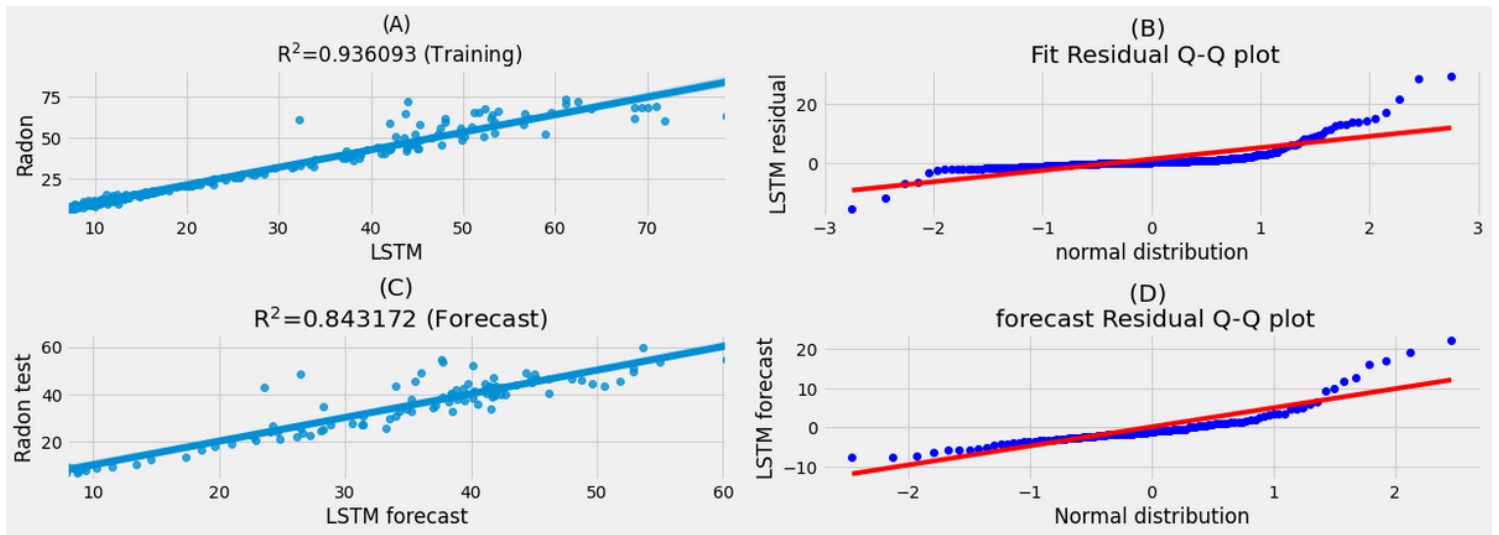
Figure 2

LSTM model diagnostics for training and testing regions,
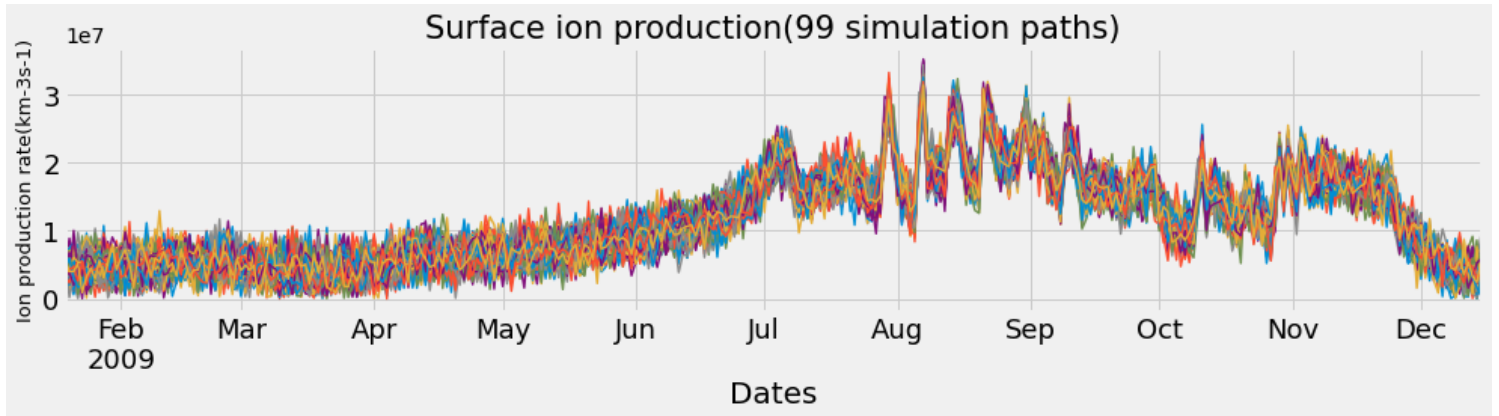
Figure 3

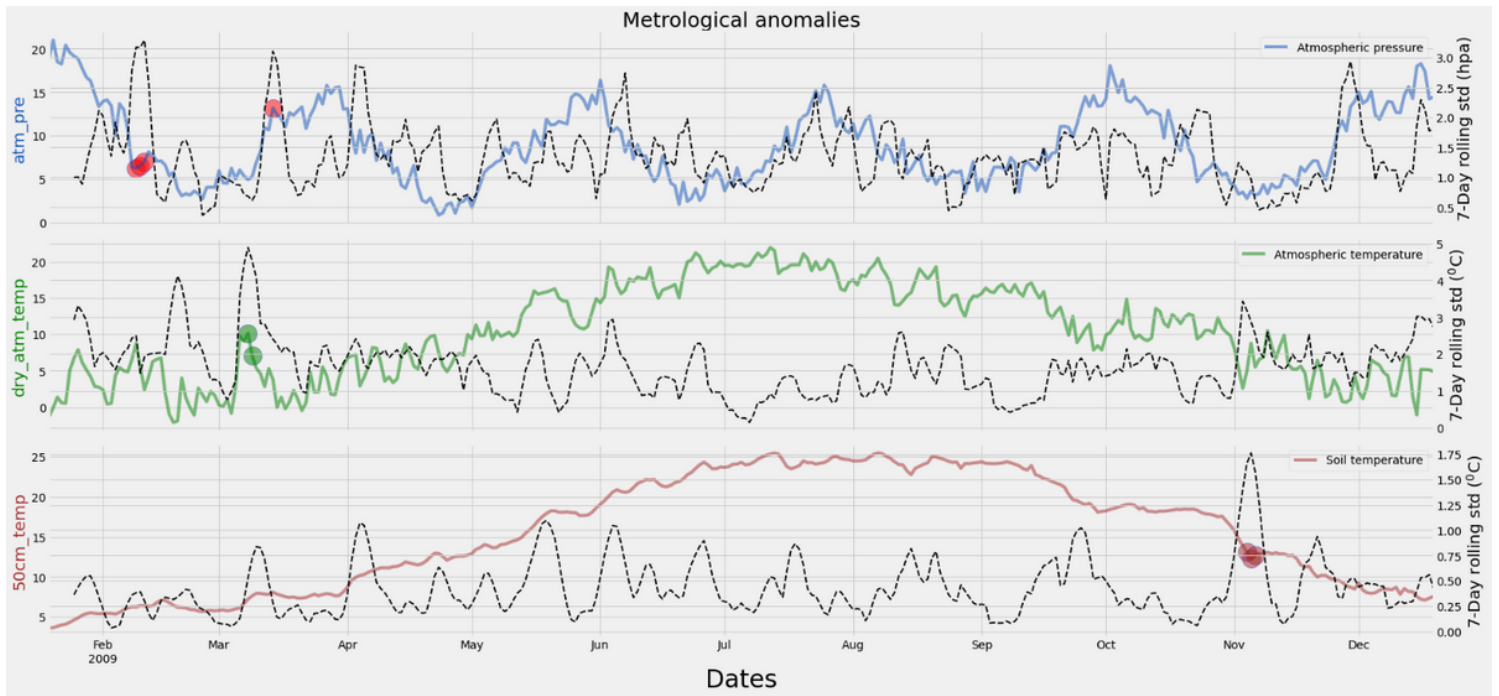Simulated surface ion production induced by Rn and its progeny during the study period,

Figure 4

50 cm soil temperature (blue curve), atmospheric temperature (green curve), and atmospheric pressure (brown curve) variations during the study period
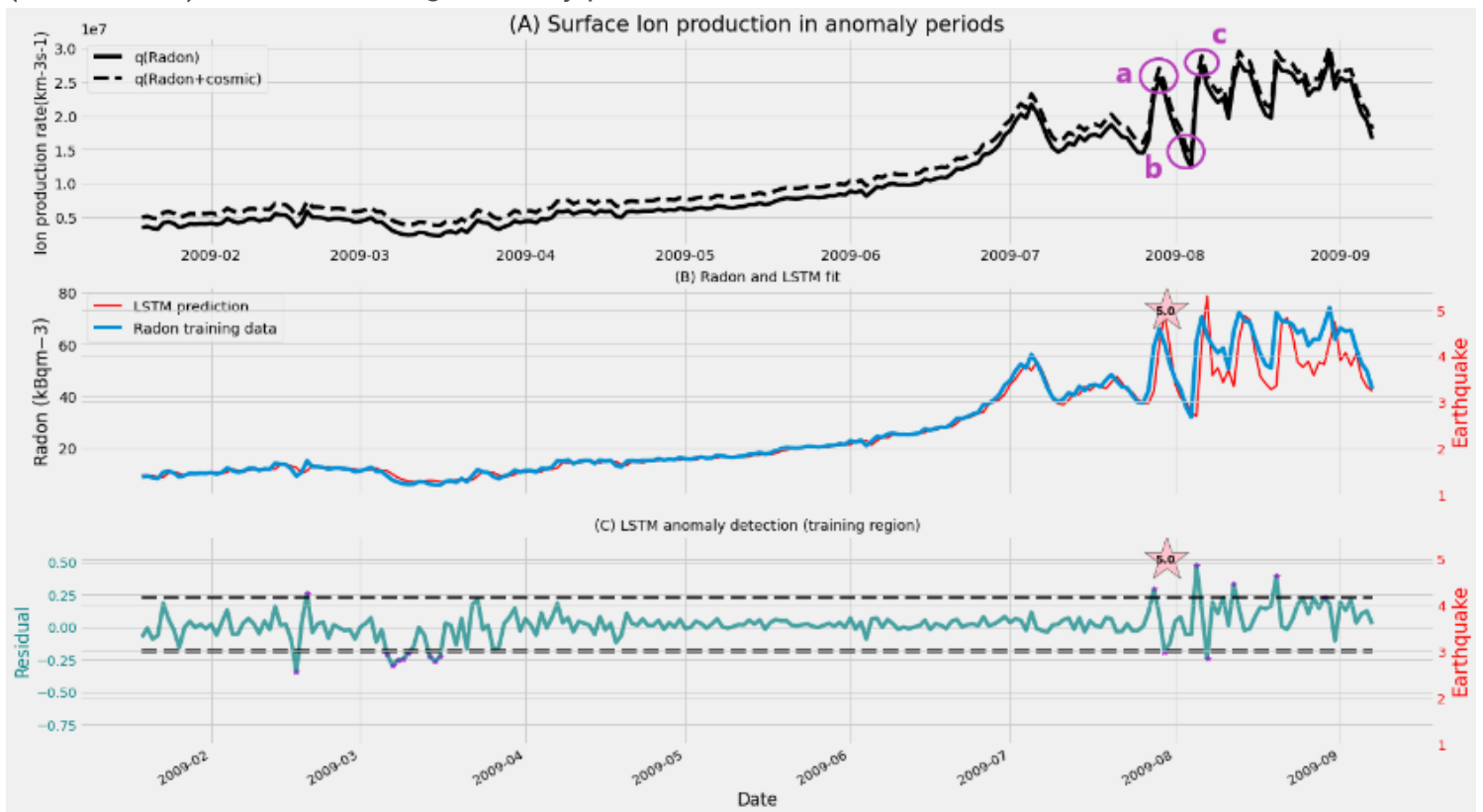

Figure 5

(A) Surface ion production due to Rn alone and Radon+Cosmic ion production, (B) Rn and LSTM fit, (C) Anomaly detection during seismic periods. The estimations in (A) were done using raw Rn data. The plots in this figure are for the training region,